WEP Warwick Evans Publishing

International Journal of Materials Science and Technology Studies

ISSN: 3006-7693 (Print), ISSN: 3006-3744 (Online) | Volume 2, Number 2, Year 2024
DOI: https://doi.org/10.62051/ijmsts.v2n2.03
Journal homepage: https://wepub.org/index.php/IJMSTS/index

Kinetic Study of the Formation Process of Ni-Zr Alloys

Weifu Cen *, Xin He

School of Material Science and Engineering, Guizhou Minzu University, Guiyang, 550025, China
*Corresponding Author: cenweifu1988@sina.cn

ABSTRACT

In this study, Ni-Zr alloy glass is chosen as the research object, and we use the molecular dynamics method to simulate and study the microstructure evolution of Ni-Zr alloy at different temperatures. The computational analysis carried out using LAMMPS, and investigated the effect of five different cold speeds on the amorphization potential of Ni-Zr. Additionally, the structural properties of Ni-Zr amorphous clusters at different cold speeds were elucidated. The results shown that cold speed is a key factor influencing the ability of Ni-Zr to form amorphous. Furthermore, amorphous formation is more likely to occur at higher cold speeds. The formation of amorphous is facilitated under the condition of higher cold speeds. By investigating the microevolutionary process and the relationship between structural entropy and temperature, it can be seen that the entropy value of the structure shows an increasing trend with the increase of temperature and cold speed. This indicates that the structure's instability increases with increasing cold speed, which is favorable to the glass-forming ability of Ni-Zr. The kinetic process and structural analysis facilitate an in-depth comprehension of the microstructural evolution law and evolution mechanism of the Ni-Zr alloy, thereby providing a more reliable theoretical basis for the application and optimization of this material.

KEYWORDS

Ni-Zr alloy; Molecular dynamics simulation; Microstructure; Rapid solidification process

1. INTRODUCTION

Amorphous alloys due to their long range of disordered atomic arrangements and short range of ordered states, amorphous alloy materials combine the properties of both glass and ordinary crystalline metals [1]. The melts of metals and alloys tend to have a crystalline structure when cooled. When metals are treated at high temperatures, the arrangement of atoms in the melt becomes irregular [2]. On cooling, an ordered and dense crystalline structure is formed. If the melt is cooled rapidly, the atoms in the melt do not have time to arrange themselves regularly and the melt becomes 'frozen', a state without rapid volume changes, resulting in an amorphous alloy or metallic glass [3]. At the microscopic level, the atomic structure affects the macroscopic properties of the alloy. Crystals and metallic glasses have different atomic arrangements, resulting in significantly different mechanical properties [4]. The unique organization of amorphous alloys gives them corrosion resistance, high strength, and good magnetic properties [5].

Nickel-zirconium binary alloys have a strong glass-forming ability and a wide range of compositions; the design of nickel-based alloy compositions usually makes the use of zirconium as the main alloying element [6], and therefore the Ni-Zr binary system has received widespread attention [7]. In recent years, with the development of science and industrial technology, many new structures have appeared in amorphous alloy systems [8]; however, the Zr-based amorphous system has attracted the attention

of many domestic and international researchers over the years due to its highly dominant glass-forming ability, high cost, and strong mechanical properties [9].

The surface composition of alloys has been extensively studied to determine the equilibrium concentrations of various constituents on undisturbed surfaces and to test displacement models. In addition, many studies have measured surface ion bombardment to determine the nature and extent of driving forces responsible for surface enrichment outside of thermodynamic processes [10]. These studies have led to a better understanding of the effects of surface atomic bonding, radiation-induced displacement, and radiation-induced diffusion on alloy surfaces. O', Connor D.J., Kang H.J., et al [11] carried out experiments in 1993 and used X-ray photoelectron spectroscopy (XPS) and differential scanning calorimetry (DSC) to determine the atomic surface bonding (ASB) effect and low energy ion scattering (LEIS) to investigate the atomic surface bonding effects [12]. LEIS was used to investigate the Zr concentration on the annealed surface of pure polycrystalline Ni-Zr samples after preferential sputtering, which was 82%, corresponding to a layer thickness of only two atomic layers [13]. The effect of oxygen during post-atmospheric cleaning was investigated, showing a gradual transition from a zirconium-enriched layer to a typically clean sputtered surface after cleaning.D. Galey et al [14] investigated the mechanism of Ni-Zr amorphization using experimental ball milling methods. There are two approaches to studying the mechanism of amorphization: static and dynamic methods [15]. To elucidate the amorphization mechanism of the ball milling method, D. Galey, L. et al. studied the microstructure of Ni-Zr during the amorphization process using transmission electron microscopy (TEM), which showed that the amorphization was the result of chemical disorder at the interface due to transverse wave scattering [16]. The work of R.W. Cochrane et al [17] investigated the surface oxidation of various Ni-Zr-rich nickel alloys to determine its role in the stability of zirconium-based amorphous metallic glasses. The evolution of the oxide film was monitored by following the XPS peaks of nickel and zirconium oxide after exposure to oxygen at 10 bar for different periods [18]. After spray cleaning, oxidation under controlled oxygen at room temperature leads to several oxidation steps to ZrO_2 and a systematic loss of surface nickel. This reaction saturates in several thousand Langmuir exposures. Throughout this process, the nickel is predominantly retained in the metallic state. Bibhu Prasad Sahu [19] et al. have systematically studied Ni-Zr alloy thin films by constant current magnetron sputtering by varying the Zr power of the target and keeping the Ni power of the target constant to study the effect of Zr content on crystallinity and microstructure evolution. The results show that by varying the Zr target power from 75 W to 175 W while keeping the Ni target power at 200 W, the Zr content of the $Ni_{1-x}Zr_x$ alloy films can be increased from 13% to 40% [20].

Zr-based amorphous systems have attracted the attention of researchers at home and abroad for many years due to their good glass-forming ability and strong mechanical properties. Dimensional stability. It has been found that the final solid solution spontaneously transforms into an amorphous state when the solvent concentration exceeds the maximum allowable value. Taichi Abe [21] et al. evaluated the liquid thermodynamics in the binary systems of Cu-Zr and Ni-Zr and estimated the critical cooling rate for glass formation by optimizing the parameter C. The results of this study show that the glass formation of Ni-Zr alloys with compositions ranging from 14% to 75% Zr is very difficult to achieve [22]. For Zr alloys, it is difficult to obtain intact bulk glass samples with a wide range of compositions and the glass forming capacity is relatively low compared to Cu and Zr alloys[23]. Therefore, their microstructures can be studied from the glass transition.

2. MODELLING

In this paper, a Lammps molecular dynamics simulation system is used to investigate the glass formation ability of Ni-Zr alloys for seven cooling conditions. These conditions are defined by the following cooling rates: $R_1=1x10^{11}$ K/s, $R_2=5x10^{11}$ K/s, $R_3=1x10^{12}$ K/s, $R_4=5x10^{12}$ K/s, $R_5=5x10^{13}$ K/s. Initially, 1000 particles were arranged in a cubic system of side length L with a composition ratio

of 1:1, and the atoms were randomly distributed on the lattice by setting the initial lattice type to an FCC structure. The periodic boundary conditions are set using the EAM potential energy function and NPT system synthesis. The kinetic process of Ni-Zr annealing to 300 K is studied for seven different cooling rates. Temperature, potential energy, position coordinates, and RDF are derived every 2000 steps throughout the process.

3. RESULTS AND DISCUSSION

3.1. Radial Distribution Function (RDF) Analysis

The radial distribution function (RDF) is used to describe the probability of finding particles from surrounding objects within a specific space. It reflects the mutual attraction or repulsion effect between particles on their distribution state. In the field of molecular simulation, it can be regarded as a method for calculating the ratio of particle density to global density inside a periodic bounding box. The objective of this paper is to present a method for calculating the number of particles within a spherical shell. The density of each spherical shell is proportional to its volume. Therefore, the regional density can be defined as the density of each spherical shell, while the local density is the ratio of the number of balls to the radius of each ball. The total number of particles within a given volume is proportional to the volume itself; thus, the global density may be defined as the density of the entire volume. When the particle radius exceeds a critical value, the constant is independent of particle size and is solely contingent on the surface roughness within the sphere, a phenomenon known as the 'interface' effect. The algorithm is presented in equation (1) [24]:

$$g(r) = \frac{\rho(r)}{\rho_0} \tag{1}$$

In the system, the regional density index of the object particle at distance r from the center particle is designated as ρ(r), while the ratio of the object particle in the global density index is also designated as ρ(r). The maximum spacing between object particles of different radii under this condition, along with the optimal scale factor corresponding to their positions, are obtained through calculation. When g(r) is equal to 1, it indicates that the regional density of the object particles at r is consistent with the global density, demonstrating a high degree of similarity.

Figures 1. (a~e) show the variation of radial distribution function of Ni-Zr alloy melt under different cooling rate conditions. Figures (a) to (e) represent the rdf of Ni-Zr alloy in the temperature range of 2500 K to 300 K. According to the figures, the g(r) curves show a consistent trend; the first and second peaks of the curves gradually increase and become narrower as the temperature decreases, which suggests that the whole system is characterized by short-range ordering. As the temperature decreases from 2500 K to 300 K, the height of the first peak of the radial distribution function gradually climbs, which indicates that the number of the first nearest neighbor atoms of each atom is increasing, thus indicating that the order of the system is gradually decreasing and the short-range disorder is gradually increasing, which suggests that the alloy has a good low-temperature performance. Figure (f) demonstrates the relationship between the height (h) of the first peak of the radial distribution function of the Ni-Zr alloy at different cooling rates and the temperature variation, showing five different sets of features. Based on these curves we obtain the law of transformation of the phase structure in this alloy with the change of cooling rate. According to the figure, with the increase of the cooling rate, the speed of the change of the first peak peaks of each component presents differences, especially at the cooling rate $R_1=1\times10^{11}$ K/s, $R_3=5\times10^{11}$ K/s and at $R_2=1\times10^{12}$ K/s, $R_4=5\times10^{12}$ K/s, the change of the second peaks is more significant, which suggests that under the condition of higher cooling rate, the amorphous formation is more easily promoted.

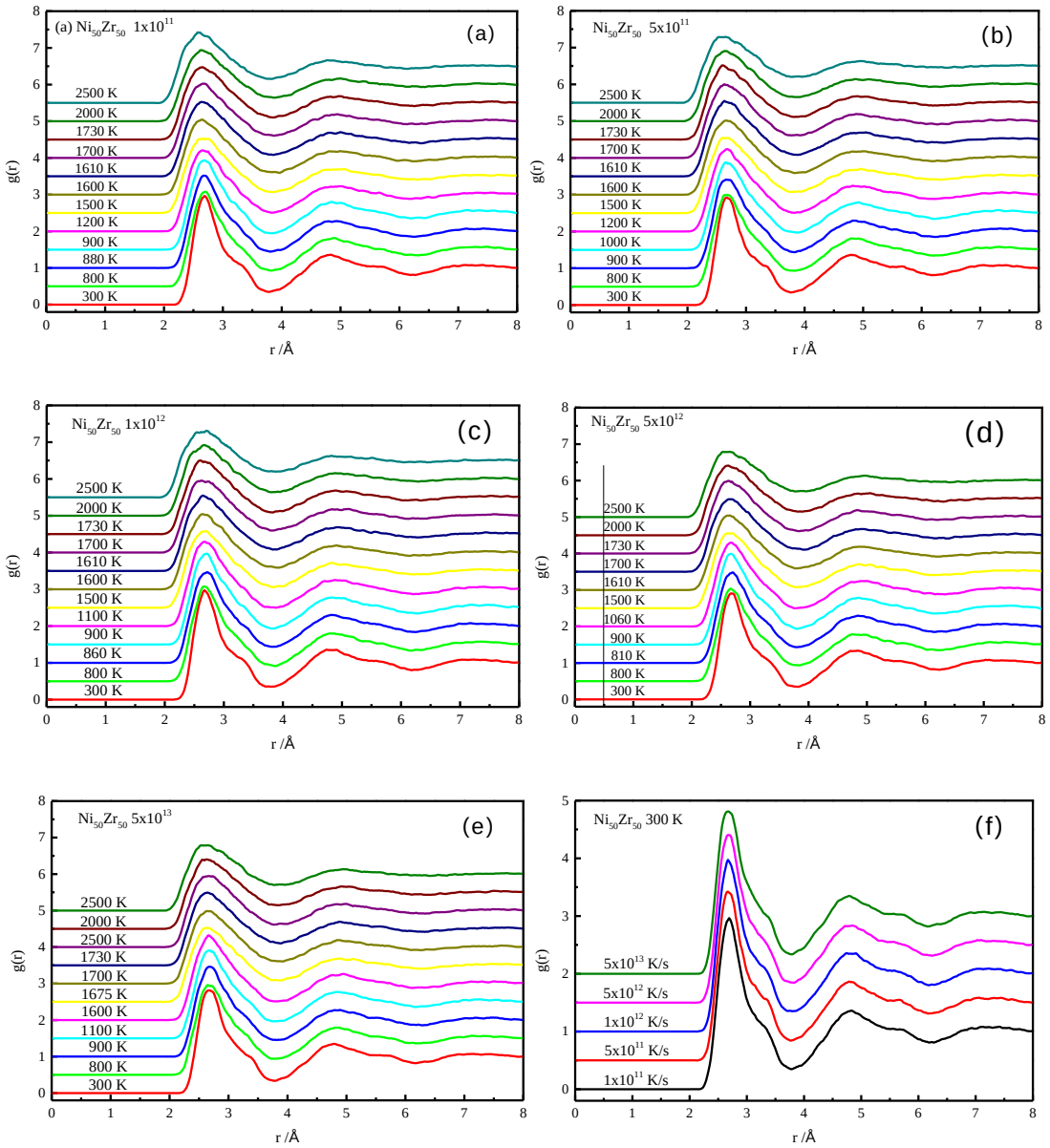

Figure 1. RDF plots of Ni-Zr alloy liquids at different cooling rates

3.2. Common Neighbourhood Cluster (CNS) Analysis

The detailed evolution of the five main CNSs in Ni-Zr alloys at varying cooling rates and temperatures is illustrated in Figure 2. The evolution of this CNS exhibits three distinct modes in response to varying temperatures.

The initial mode of evolution is characterized by a gradual decrease in the number of S444, S555, and S666 [25], as a consequence of the cooling rate. This is observed in the cooling rates R_1=1x10^{11} K/s, R_2=1x10^{12} K/s, R_3=1x10^{12} K/s, R_4=5x10^{12} K/s, and R_5=5x10^{13} K/s (see Figs. (a~e)). The second pattern is characterized by a gradual increase in the number of S311, S322, S421, S422, S433 and S655 at cooling rates R_1=1x10^{11} K/s, R_2=5x10^{11} K/s, R_3=1x10^{12} K/s, R_4=5x10^{12} K/s and R_5=5x10^{13} K/s (see Figs. (a~e)) exhibited a gradual increase. The number of S544 undergoes a process of increasing and then decreasing, finally reaching its maximum value (of 17.78%) at R_5 = 5x10^{13} K/s, followed by corresponding decreases around 1300 K and 1750 K, as detailed in Figure 2(a~e).

Among the five major CNSs, S555 exhibits no translational symmetry and a high degree of rotational symmetry, which is an inherent property of metallic glasses or topologically close-packed crystals. S544 and S433 can be readily deformed in S555 and S444, respectively, which are considered to be

the primary structures of metallic glasses [26]. At a temperature of 300 K and a cooling rate of R_5= 5x10^{13} K/s, the maximum content of S555 can reach 34.86%. The maximum content of S444 and S666 is approximately 8.87% and 12.95%, respectively, at a cooling rate of R_5=5x10^{13} K/s. The quantity of S433 demonstrates a gradual increase in the cooling rate of R_2, R_3, R_4, R_5. However, the maximum content at a cooling rate of R_5=5x10^{13} K/s is 15.15%. S544, on the other hand, exhibits a downward trend in its content after a certain temperature, but reaches its maximum content at the cooling rate of R_5=5x10^{13} K/s, with a value of 17.78%. It can thus be concluded that an appropriate increase in the cooling rate can assist NiZr alloys in enhancing their glass formation ability (GFA).

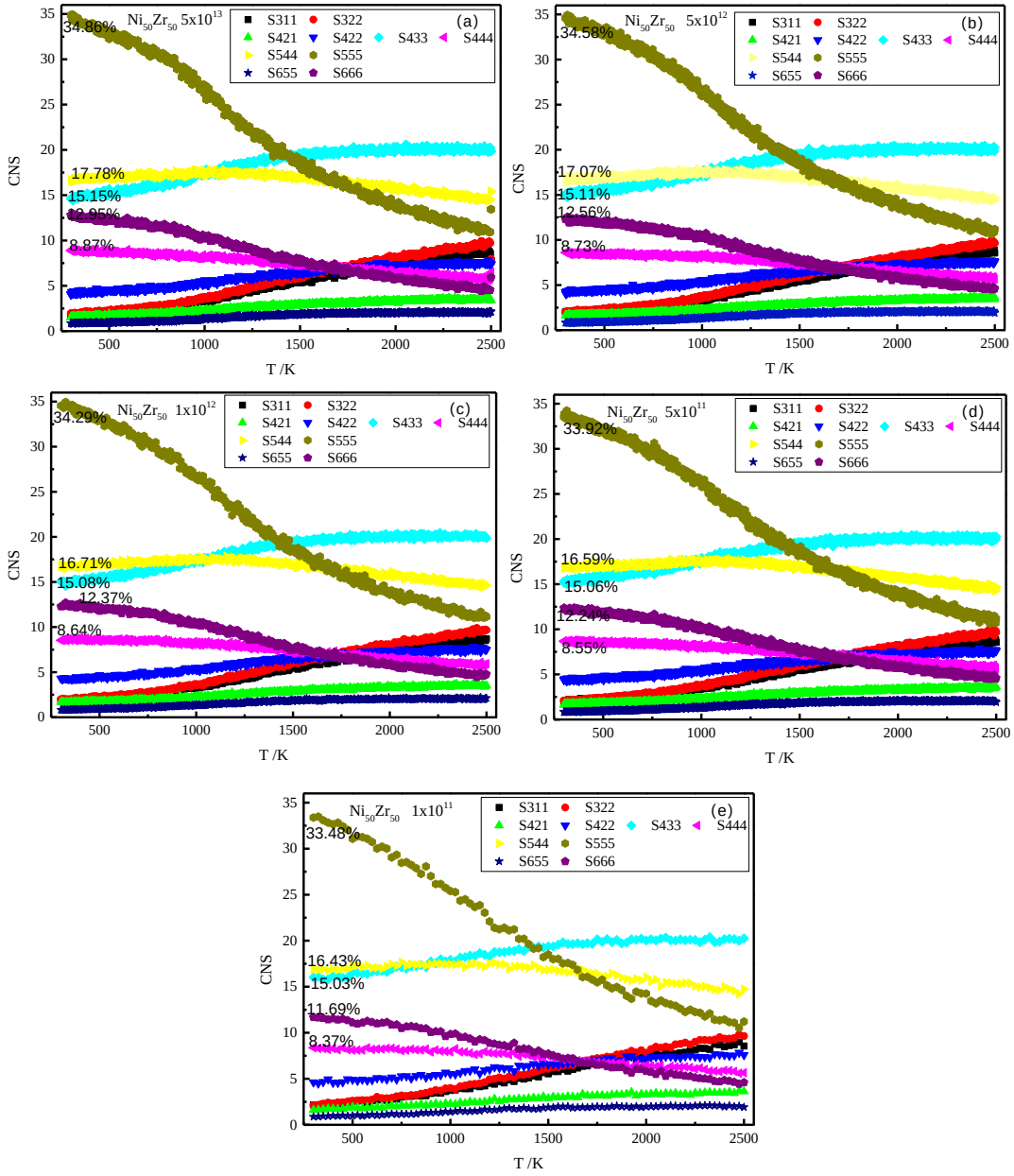

Figure 2. the function of CNS and temperture at different cooling speeds

3.3. Structural Entropy Analysis

Entropy reflects the degree of chaos in a system and is a state function in a physical system. It is widely believed that the higher the entropy value, the more chaotic the system. A higher entropy value means that the system energy distribution is more uniform, the better the thermodynamic stability, and the material system within the disordered liquid and amorphous structure entropy value is generally greater than the crystal structure entropy value. In order to provide a more detailed analysis

and description of the structural changes occurring within the system, the concept of LaSC structure is employed. This allows for the examination and documentation of the various local topological structure types and their associated probability distributions. The structural entropy during solidification represents the difference between the entropy of the supercooled liquid and the crystal within the system, which is related to the discrete positions of the system atoms. Furthermore, the structural entropy during melting is defined as a parameter capable of reflecting the degree of structural ordering of the melting process system, as illustrated by equation (2) [27].

$$S = -\sum(\rho_i \log \rho_i) \tag{2}$$

Since this type of structure makes up a large proportion of the system, its value is less than 1. For the system containing only one type of LaSC structure, we can infer that its S = 0. Looking at this result, we find that the conclusion does not fully correspond to the actual situation. As the number of structural types of the system increases, its size will gradually decrease and the value of S will increase, which will lead to the deepening of the disorder of the system. The relationship between the structural types of LaSC structures and the degree of orderliness of the system can be determined by the Maximum Criteria Cluster Analysis (MCCA), which is an extremely important method for structural analysis.

Figure 3 shows the structural entropy curves of five groups with temperature change under different cooling rate conditions. Figure 4 shows the CNS structural entropy of NiZr, Figure 5 shows the CN structural entropy of NiZr, Figure 6 shows the structural entropy of LSC of NiZr, and Figure 7 shows the types of LSC. From the figure, the LSC has a higher structural entropy of more than 1. 95 for a cooling rate of $R_5 = 5\times10^{13}$ K/s, indicating that there is a wide variety of initial structures of the system, which since the LSC analysis method is able to classify the disordered liquid structures more finely. It also shows that there is a relationship between the cooling rate and the structural entropy at low temperatures. As the temperature increases, the entropy value of the structure shows a maximum value when the cooling rate condition is $R_5=5\times10^{13}$ K/s, indicating that the instability of the structure increases as the cooling rate increases. This is due to the presence of many grain boundaries in the polycrystalline structure and the continuous melting of the grain boundaries during the heating process leads to the maximum value of the structural entropy. It also indicates the presence of a large number of crystals with small grain sizes and low density in the system at low temperatures, and the appearance of these crystal defects at high temperatures complicates the system. When the temperature exceeds 500 K, the entropy value shows an almost linear increasing trend, which is well reflected in the fitted curves.

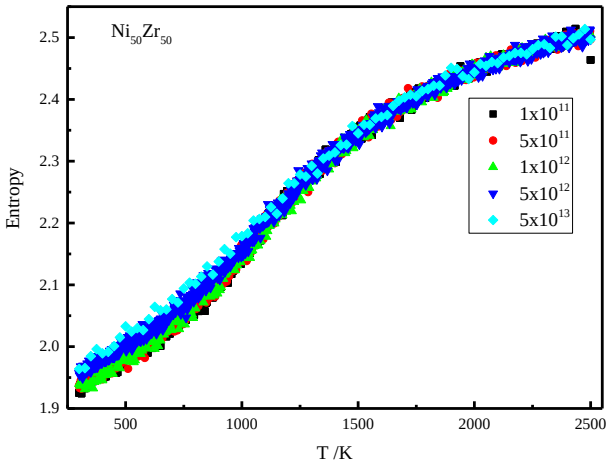

Figure 3. Plot of entropy as a function of temperature

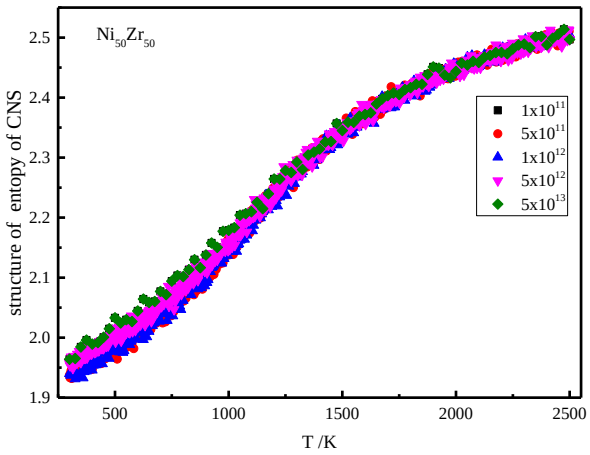

Figure 4. Structural entropy of CNS

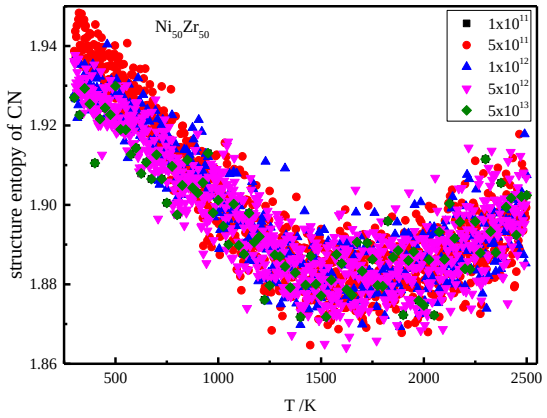

Figure 5. Structure entropy of CN

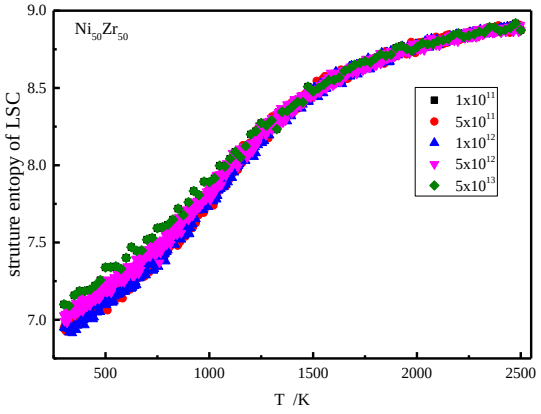

Figure 6. Structural entropy of LSC

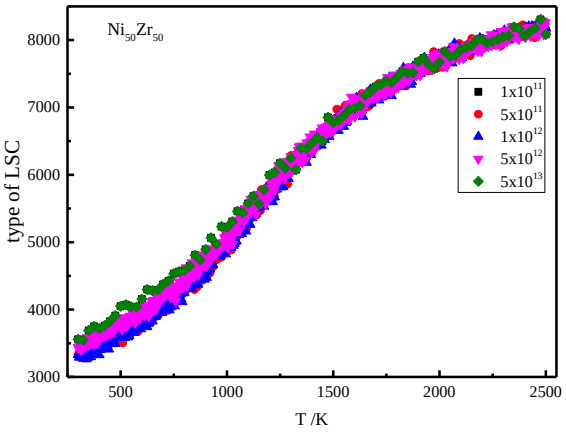

Figure 7. the types of LSC

3.4. Crystallographic Phase Transition

The average energy of atoms is a basic statistical parameter of the system, and its characteristic change with temperature can reflect the basic types of phase transitions, thus revealing the nature of phase transitions. In this paper, a set of models based on interatomic forces and electronic structure theory is established to calculate the average energy of atoms using the molecular dynamics simulation method. The thermodynamic properties of metal alloys in the stages of melting,

crystallization, and supercooled melt, as well as their influence on the variation rule of the atomic mean energy with time, are investigated by measuring the plots of the atomic mean energy versus temperature at different cooling rates. The solidification process of liquid Ni-Zr nanoparticles shows a curve of atomic mean energy as the temperature (E-T) changes.

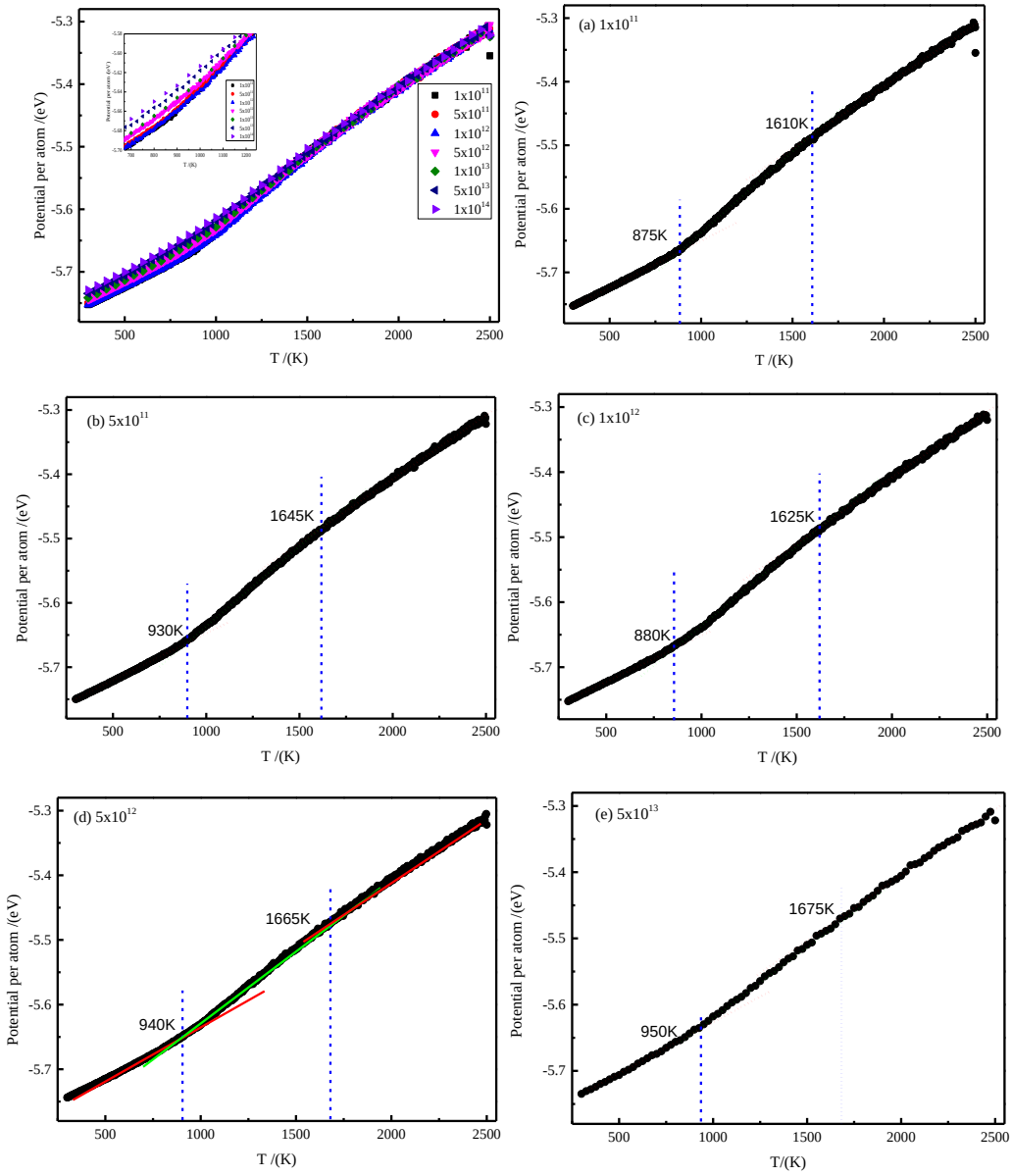

Figure 8. the potential energy curve with different cooling condition

We have quenched liquid samples of Ni-Zr melted at high temperatures up to 300 K. In our experiments, a monotonically decreasing trend of the atomic potential energy with decreasing temperature was found, which is related to the atomic arrangement during the phase transition. A close correlation between atomic potential energy and temperature was observed for the Ni-Zr alloys (each with 50% content) under five different sets of cooling conditions. As the cooling rate increases in the two groups of R_1 and R_3, the glass transition temperature of the glass gradually increases, with Tg values of 875 K and 880 K respectively; in the three groups of cooling rates of R_2, R_4 and R_5, the Tg values are 930 K, 940 K and 950 K respectively, indicating that the glass transition is closely related to the cooling rate. As the cooling rate increases, the Tg values obtained also increase. As the system moves away from the steady state, the glass transition starts later and later as the cooling rate increases, eventually reaching an equilibrium value where the phase transition point from low to high temperature is slightly higher than it would otherwise be. At higher temperatures, a tendency towards a more glassy state is inevitable as the system is unable to repair itself to form an irregular solid. As

the cooling rate increases, the tendency to form a glassy transition increases, leading to a shift in Tg towards higher temperatures.

4. SUMMARY

The formation mechanism of the amorphous organization under certain cooling rate conditions has been investigated by molecular dynamics methods. For the amorphous Ni-Zr alloy, a detailed analytical study was carried out at different cooling rates. The evolution trends of proximity subclusters and glass transition temperatures were observed during rapid solidification, and the conclusions are as follows.

(1) From the two-body distribution function (RDF) under different cooling rate conditions, it can be seen that the amorphous formation is more likely to be promoted under higher cooling rate conditions.

(2) At a cooling rate of $5x10^{13}$ K/s, the content of all structure types is higher than the rest of the cooling rate because the precipitated phase species increase and are more uniformly distributed in the alloy with increasing cooling rate. Therefore, a moderate increase in the cooling rate can effectively enhance the glass formation ability (GFA) of NiZr alloys, thus improving their properties. Meanwhile, the relationships between sub-clusters under different cooling rates are found to decrease the distance between sub-clusters with increasing cooling rates, leading to an increase in density.

(3) With the gradual decrease in temperature, the potential energy of the Ni-Zr alloy samples shows a decreasing trend under all five sets of different cooling rate conditions. With the increase in cooling rate, the glass transition temperature of the system also shows a gradually increasing trend. The experiments show that the Tg values obtained at higher cooling rate conditions show a positive correlation trend, while the Tg values obtained at lower cooling rate conditions show a negative correlation. As the cooling rate increases, the cooling rate of the system is also accelerated, which leads to a natural increase in the glass transition temperature, which in turn promotes the formation of the glassy state, therefore the glass transition occurs at higher temperatures.

ACKNOWLEDGEMENTS

This work was supported by the PhD initial foundation of Guizhou MinZu University (GZMUZK[2024]QD17), the Youth Science and Technology Talents Growth Fund Program of the Ministry of Education Province, China (NO.[2022]155).

REFERENCES

[1] Xu, S.; Jia, F.; Zhao, G.; Wu, W.; Ren, W. A Two-Dimensional Ferroelectric Ferromagnetic Half Semiconductor in a VOF Monolayer. J. Mater. Chem. C 2021, 9 (29), 9130–9136. https://doi.org/10.1039/D1TC02238E

[2] Sethulakshmi, N.; Mishra, A.; Ajayan, P. M.; Kawazoe, Y.; Roy, A. K.; Singh, A. K.; Tiwary, C. S. Magnetism in Two-Dimensional Materials beyond Graphene. Materials Today. 2019, 27, 107–122. https://doi.org/10.1016/j.mattod.2019.03.015

[3] Wang Q.H.; Amilcar B.P.; Mark B.; Avalon H.D. The Magnetic Genome of Two-Dimensional van der Waals Materials. ACS Nano. 2022, 16: 6960-7079. https://pubs.acs.org/doi/full/ 10.1021/acsnano.1c09150

[4] Lu, M.; Yao, Q.; Li, Q.; Xiao, C.; Huang, C.; Kan, E. Tuning Electronic and Magnetic Properties of Two-Dimensional Ferromagnetic Semiconductor CrI3 through Adsorption of Benzene. J. Phys. Chem. C 2020, 124 (40), 22143–22149. https://doi.org/10.1021/acs. jpcc.0c06071

[5] Si C.; Zhou, J.; Sun, Z. Half-Metallic Ferromagnetism and Surface Functionalization-Induced Metal–Insulator Transition in Graphene-like Two-Dimensional Cr2C Crystals. ACS Appl. Mater. Interfaces 2015, 7 (31), 17510–17515. https://doi.org/10.1021/acsami.5b05401

[6] Liu, J.; Shi, M.; Lu, J.; Anantram, M. P. Analysis of Electrical-Field-Dependent Dzyaloshinskii-Moriya Interaction and Magnetocrystalline Anisotropy in a Two-Dimensional Ferromagnetic Monolayer. Phys. Rev. B 2018, 97 (5), 054416. https://doi.org/10.1103/ PhysRevB.97.054416

[7] Wu, M.; Zeng, X. C. Intrinsic Ferroelasticity and/or Multiferroicity in Two-Dimensional Phosphorene and Phosphorene Analogues. Nano Lett. 2016, 16 (5), 3236–3241. https://doi.org/10.1021/acs.nanolett.6b00726

[8] Lei, Z.; Sathish, C. I.; Geng, X.; Guan, X.; Liu, Y.; Wang, L.; Qiao, L.; Vinu, A.; Yi, J. Manipulation of Ferromagnetism in Intrinsic Two-Dimensional Magnetic and Nonmagnetic Materials. Matter 2022, 5 (12), 4212–4273. https://doi.org/10.1016/j.matt.2022.11.017

[9] Wang, B.; Zhang, X.; Zhang, Y.; Yuan, S.; Guo, Y.; Dong, S.; Wang, J. Prediction of a Two-Dimensional High- TC f-Electron Ferromagnetic Semiconductor. Mater. Horiz. 2020, 7 (6), 1623–1630. https://doi.org/10.1039/D0MH00183J

[10] Huang, P.; Zhang, P.; Xu, S.; Wang, H.; Zhang, X.; Zhang, H. Recent Advances in Two-Dimensional Ferromagnetism: Materials Synthesis, Physical Properties and Device Applications. Nanoscale 2020, 12 (4), 2309–2327. https://doi.org/10.1039/C9NR08890C

[11] David L.C; Grace L.C.; Causer K.C.; Helmut F.; Wolfgang K.; Frank K. Two-Dimensional Magnets: Forgotten History and Recent Progress towards Spintronic Applications. Advanced functional materials. 2020, 30, 1901414. https://onlinelibrary.wiley.com/doi/epdf/10.1002/ adfm.201901414

[12] Blügel, S. Two-Dimensional Ferromagnetism of 3 d, 4 d, and 5 d Transition Metal Monolayers on Noble Metal (001) Substrates. Phys. Rev. Lett. 1992, 68 (6), 851–854. https://doi.org/ 10.1103/PhysRevLett.68.851

[13] Wang, M.; Kang, L.; Su, J.; Zhang, L.; Dai, H.; Cheng, H.; Han, X.; Zhai, T.; Liu, Z.; Han, J. Two-Dimensional Ferromagnetism in CrTe Flakes down to Atomically Thin Layers. Nanoscale 2020, 12 (31), 16427–16432. https://doi.org/10.1039/D0NR04108D

[14] Wang, B.; Zhang, X.; Zhang, Y.; Yuan, S.; Guo, Y.; Dong, S.; Wang, J. Prediction of a Two-Dimensional High- TC f-Electron Ferromagnetic Semiconductor. Mater. Horiz. 2020, 7 (6), 1623–1630. https://doi.org/10.1039/D0MH00183J

[15] Li, Z.; Cao, T.; Louie, S. G. Two-Dimensional Ferromagnetism in Few-Layer van Der Waals Crystals: Renormalized Spin-Wave Theory and Calculations. Journal of Magnetism and Magnetic Materials 2018, 463, 28–35. https://doi.org/10.1016/j.jmmm.2018.04.064

[16] Jiang, S.; Shan, J.; Mak, K. F. Electric-Field Switching of Two-Dimensional van Der Waals Magnets. Nature Mater 2018, 17 (5), 406–410. https://doi.org/10.1038/s41563-018-0040-6

[17] Khan, I.; Marfoua, B.; Hong, J. Electric Field Induced Giant Valley Polarization in Two Dimensional Ferromagnetic WSe2/CrSnSe3 Heterostructure. npj 2D Mater Appl 2021, 5 (1), 1–8. https://doi.org/10.1038/s41699-020-00195-9

[18] You, J.-Y.; Dong, X.-J.; Gu, B.; Su, G. Electric Field Induced Topological Phase Transition and Large Enhancements of Spin-Orbit Coupling and Curie Temperature in Two-Dimensional Ferromagnetic Semiconductors. Phys. Rev. B 2021, 103 (10), 104403. https://doi.org/10.1103/ PhysRevB.103.104403

[19] Choi, J. S.; Yoo, J. Simultaneous Structural Topology Optimization of Electromagnetic Sources and Ferromagnetic Materials. Computer Methods in Applied Mechanics and Engineering 2009, 198 (27), 2111–2121. https://doi.org/10.1016/j.cma.2009.02.015

[20] Guo, Y.; Zhang, Y.; Zhou, Z.; Zhang, X.; Wang, B.; Yuan, S.; Dong, S.; Wang, J. Spin-Constrained Optoelectronic Functionality in Two-Dimensional Ferromagnetic Semiconductor Heterojunctions. Mater. Horiz. 2021, 8 (4), 1323–1333. https://doi.org/10.1039/D0MH01480J

[21] Khan, I.; Marfoua, B.; Hong, J. Electric Field Induced Giant Valley Polarization in Two Dimensional Ferromagnetic WSe2/CrSnSe3 Heterostructure. npj 2D Mater Appl 2021, 5 (1), 1–8. https://doi.org/10.1038/s41699-020-00195-9

[22] Guo Y, Wang B, Zhang X, Yuan S, Ma L, Wang J, Magnetic two-dimensional layered crystals meet with ferromagnetic semiconductors, InfoMat, 2020, 2(4): 639-655. https://onlinelibrary.wiley.com/doi/epdf/10.1002/inf2.12096

[23] Wang, M.; Kang, L.; Su, J.; Zhang, L.; Dai, H.; Cheng, H.; Han, X.; Zhai, T.; Liu, Z.; Han, J. Two-Dimensional Ferromagnetism in CrTe Flakes down to Atomically Thin Layers. Nanoscale 2020, 12 (31), 16427–16432. https://doi.org/10.1039/D0NR04108D

[24] Du, J.; Wen, B.; Melnik, R.; Kawazoe, Y. First-Principles Studies on Structural, Mechanical, Thermodynamic and Electronic Properties of Ni–Zr Intermetallic Compounds. Intermetallics. 2014, 54, 110–119. https://doi.org/10.1016/j.intermet.2014.05.021

[25] Zhang, C.; Yan, S. First-Principles Study of Ferromagnetism in Two-Dimensional Silicene with Hydrogenation. J. Phys. Chem. C. 2012, 116 (6), 4163–4166. https://doi.org/ 10.1021/ jp2104177

[26] Yang, K.; Fan, F.; Wang, H.; Khomskii, D. I.; Wu, H. VI 3 : A Two-Dimensional Ising Ferromagnet. Phys. Rev. B 2020, 101 (10), 100402. https://doi.org/10.1103/ PhysRevB. 101.100402

[27] Tian, Y.; Gray, M. J.; Ji, H.; Cava, R. J.; Burch, K. S. Magneto-Elastic Coupling in a Potential Ferromagnetic 2D Atomic Crystal. 2D Mater. 2016, 3 (2), 025035. https://doi.org/10.1088/ 2053-1583/3/2/025035